*J. Fluid Mech.* (2013), *vol.* 733, *pp.* 245–267. © Cambridge University Press 2013 
doi:10.1017/jfm.2013.415

# Gyrotactic bioconvection at pycnoclines

**A. Karimi† and A. M. Ardekani**

Department of Aerospace and Mechanical Engineering, University of Notre Dame, Notre Dame, IN 46556, USA

(Received 21 January 2013; revised 26 June 2013; accepted 8 August 2013; first published online 26 September 2013)

Bioconvection is an important phenomenon in aquatic environments, affecting the spatial distribution of motile micro-organisms and enhancing mixing within the fluid. However, stratification arising from thermal or solutal gradients can play a pivotal role in suppressing the bioconvective flows, leading to the aggregation of micro-organisms and growth of their patchiness. We investigate the combined effects by considering gyrotactic motility where the up-swimming cells are directed by the balance of the viscous and gravitational torques. To study this system, we employ a continuum model consisting of Navier–Stokes equations with the Boussinesq approximation coupled with two conservation equations for the concentration of cells and stratification agent. We present a linear stability analysis to determine the onset of bioconvection for different flow parameters. Also, using large-scale numerical simulations, we explore different regimes of the flow by varying the corresponding boundary conditions and dimensionless variables such as Rayleigh number and Lewis number ($Le$) and we show that the cell distribution can be characterized using the ratio of the buoyancy forces as the determinant parameter when $Le < 1$ and the boundaries are insulated. But, in thermally stratified fluids corresponding to $Le > 1$, temperature gradients are demonstrated to have little impact on the bioconvective plumes provided that the walls are thermally insulated. In addition, we analyse the dynamical behaviour of the system in the case of persistent pycnoclines corresponding to constant salinity boundary conditions and we discuss the associated inhibition threshold of bioconvection in the light of the stability of linearized solutions.

**Key words:** bioconvection, buoyancy-driven instability, stratified flows

## 1. Introduction

Many aquatic and marine environments are characterized by vertical variations in water density, termed pycnoclines, which have a great impact on the biological activities. During the past few decades, important correlations have been discovered between regions of fluid stratification and a wide range of environmental processes, including algal blooms, accumulation of marine snow particles, and hindering of vertical migration of aquatic organisms (Alldredge & Gotschalk 1989; Bergström & Strömberg 1997; Sherman *et al.* 1998; Jephson & Carlsson 2009). Despite this, the fundamental fluid dynamics of swimming in a stratified fluid have remained largely unexplored. This is partly due to the widespread belief that the relevant length scale

† Email address for correspondence: akarimi@nd.edu

https://doi.org/10.1017/jfm.2013.415 Published online by Cambridge University Press

of stratification is orders of magnitude larger than the organisms. This notion was recently refuted and it was shown (Ardekani & Stocker 2010) that typical aquatic stratifications can in fact affect the flow field of particles and organisms as small as $O(100\ \mu\text{m}–1\ \text{mm})$. Employing numerically resolved calculations of swimming in stratified fluids, Doostmohammadi, Stocker & Ardekani (2012) demonstrated that the flow field generated by swimmers and consequently their ecology are indeed strongly affected by density stratification. Here in this paper, we discuss different physical phenomena where density stratification hinders bioconvection and leads to aggregation of micro-organisms and formation of algal blooms.

Bioconvection patterns are observed in cultures of swimming micro-organisms which are heavier than water and tend to propel themselves toward the upper surface of their environment in response to external stimuli such as gravity, light, and chemical gradient. As a consequence, a heavy layer of cells appears on top of the lighter fluid which can initiate an overturning instability similar to Rayleigh–Bénard convection, and thus producing spatially extended patterns maintained by return upward swimming of the micro-organisms (Hill & Pedley 2005). This phenomenon can be found in bacterial, flagellate, plankton and ciliate cultures (Plesset & Winet 1974). We are interested in gyrotaxis where the swimming direction is dictated by the balance of the gravitational torque acting on a bottom-heavy cell and viscous torque exerted by the local shear flow (Kessler 1985). It causes the formation of plumes of cells in deep vessels by orienting the cells' swimming velocity towards the regions of downwelling fluid as depicted in experimental images (Kessler 1986; Pedley & Kessler 1992).

Observations of pattern formation in bioconvection have been recorded previously in several studies, for example by Loefer & Mefferd (1952), Wille & Ehret (1968), and Kessler (1984), but the results were of only qualitative importance. Bees & Hill (1997) for the first time quantitatively analysed the patterns formed in shallow suspensions of the alga *Chlamydomonas nivalis* by measuring the corresponding pattern wavelength as a function of depth and cell concentration using two-dimensional Fourier transforms of the experimental images. This type of bioconvective pattern has also been observed for other kinds of micro-organisms. For example, Yamamoto *et al.* (1992) studied the effects of depth and concentration on the patterns formed in suspensions of *C. reinhardtii*, and Mendelson (1999) focused on the multicellular states in the complex colonies and bioconvection patterns produced by *Bacillus subtilis*.

Pedley, Hill & Kessler (1988) developed the first continuum model governing the gyrotactic instability of a uniform suspension of bottom-heavy swimming cells. They assumed that the cells are identical spheroids, each swimming at the same prescribed speed relative to the fluid in a direction governed deterministically by the gyrotactic torque balance. However, they postulated the cell diffusivity, representing the randomness of the motility behaviour, as a constant isotropic tensor which is inconsistent with the assumption of deterministic swimming orientation. This continuum model has been employed to carry out numerical simulations of the gyrotactic bioconvection in two-dimensional periodic domains (Ghorai & Hill 2000) and in the three-dimensional deep rectangular chambers with stress-free sidewalls (Ghorai & Hill 2007). Pedley & Kessler (1990) improved the aforementioned model by incorporating a probability density function of swimming direction governed by a quasi-steady Fokker–Planck equation in order to compute the random fluctuations in the orientation of the micro-organisms. Even so, their proposed expression for the diffusion tensor was *ad hoc* and remained valid only in the limit of asymptotically weak shear flow. To overcome this difficulty, Hill & Bees (2002) and Manela &

https://doi.org/10.1017/jfm.2013.415 Published online by Cambridge University Press

Frankel (2003) calculated the diffusion tensor using the generalized Taylor dispersion theory which accounts for shear-induced contributions in both the cells' position and orientation. This approach has been employed to simulate suspensions of swimming micro-organisms subjected to a range of shear strengths in planar (Bearon, Hazel & Thorn 2011) and axisymmetric pipe flows (Bearon, Bees & Croze 2012) and the corresponding results exhibit good agreement with those obtained via individual-level biased random walk simulations.

Particle models have been also used in multiple studies of the collective behaviour of micro-organisms. Hopkins & Fauci (2002) constructed a combined Eulerian–Lagrangian numerical framework to simulate bioconvection in which the motion of individual cells is tracked. Moreover, Thorn & Bearon (2010) compared the deterministic and stochastic approaches to determine the swimming direction by Lagrangian tracking of particulate micro-organisms in quiescent fluid and homogeneous shear flow. A potential drawback of these models is the computational limitations in tracking a sufficient number of cells needed to make direct comparisons with experiments.

Bioconvection can play an important role in influencing the distribution of micro-organisms and enhancing mixing within the fluid in natural environments (Pedley & Kessler 1992). In this phenomenon, the accumulation of the micro-organisms occurs due to the presence of physical stimuli, such as gravity (Kessler 1985), light intensity (Ghorai, Panda & Hill 2010), and chemical gradients (Hillesdon, Pedley & Kessler 1995; Hillesdon & Pedley 1996), which direct the preferred swimming orientation of the cells. The resulting non-uniform cell distribution combined with the density difference between the cells and surrounding fluid lead to an unstable stratification which generates large-scale convective flows. However, other biological and physical factors may affect the pattern formation and aggregation of the cells. In particular, density stratification caused by thermal or solutal gradients could have a great impact on the cells' spatial distribution. Experimental observations have demonstrated that establishment of stable salinity stratification can suppress bioconvection and its induced mixing, leading to the formation of harmful algal blooms of *Heterosigma akashiwo* (Hershberger *et al.* 1997; Bearon & Grunbaum 2006). Also, the population dynamics of the phytoplankton blooms in the aquatic environments is largely influenced by the oceanic density-stratified flows (Smayda 1997). In these examples, two buoyancy forces arising from the bioconvection and stratification compete with each other and the regime of the flow depends on their relative magnitude and direction.

In the current study, we investigate the combined effects of density gradients engendered by the gyrotactic motility of the micro-organisms and solutal/thermal stratification. Despite being reminiscent of the phenomenon of double diffusion (Turner 1973; Huppert & Turner 1981), this system functions distinctively due to the stratification of one of the components being caused by active swimming of the cells. We also analyse how the interaction of these stratified agents affects the cell patchiness and mixing in the fluid flow. Employing large-scale three-dimensional numerical simulations performed for the first time, we explore different regimes of the flow within the parameter space of the system. The remainder of the paper is organized as follows. In § 2, we describe the governing equations and the dimensionless numbers. In § 3, we outline the numerical approach used to compute the flow field. In § 4, we carry out the linear stability analysis of the problem and identify the corresponding criteria for transition to instability. In § 5, we present our

https://doi.org/10.1017/jfm.2013.415 Published online by Cambridge University Press

numerical results and discuss the interaction of salinity gradient and bioconvection. Concluding remarks are given in § 6.

## 2. Mathematical formulation

### 2.1. *Governing equations*

Following the framework presented by Pedley *et al.* (1988), we assume a dilute suspension of cells modelled by a continuous distribution. Thus, denoting the concentration (number density) of cells by $n(\boldsymbol{x}, t)$, we have $nv \ll 1$ where $v$ is the average volume of a cell. The bulk fluid velocity $\boldsymbol{u}$ is subject to the continuity and Navier–Stokes equations with the Boussinesq approximation in which the cell concentration and salinity stratification alter the fluid density linearly through buoyancy terms:

$$\boldsymbol{\nabla} \cdot \boldsymbol{u} = 0, \tag{2.1}$$

$$\rho \left( \frac{\partial \boldsymbol{u}}{\partial t} + \boldsymbol{u} \cdot \boldsymbol{\nabla} \boldsymbol{u} \right) = -\boldsymbol{\nabla} p_e + (\rho \beta (S - S_0) + nv \Delta \rho)\, \boldsymbol{g} + \mu \nabla^2 \boldsymbol{u}, \tag{2.2}$$

where $\rho$ is the background fluid density, $\Delta\rho$ is the excess density of the cells ($\Delta\rho \ll \rho$), $\mu$ is the fluid viscosity, $p_e$ is the pressure excess over hydrostatic, and $\boldsymbol{g} = -g\hat{\boldsymbol{z}}$ is the gravitational acceleration vector which throughout this study is assumed to be in the negative-$z$ direction. The salinity is denoted by $S$, with $S_0$ being the reference value and $\beta$ the corresponding coefficient of expansion. In the case of thermal stratification, the buoyancy force retains the same format with $S$ representing temperature and $\beta$ the thermal expansion coefficient.

Here, we neglect cell division due to its longer time scale compared to bioconvective flows. For example in the case of *Heterosigma akashiwo* cells, the division cycle takes about a day, but their descending plumes resulting from the bioconvection develop in less than 5 min (Bearon & Grunbaum 2006). Hence, the cell conservation equation can be represented as

$$\frac{\partial n}{\partial t} = -\boldsymbol{\nabla} \cdot \boldsymbol{J}, \tag{2.3}$$

where the flux of the cells is $\boldsymbol{J} = n\boldsymbol{u} + nW_c \boldsymbol{p} - D\boldsymbol{\nabla} n$. Here, $W_c$ is the constant swimming speed of the cells, $\boldsymbol{p}$ is the unit vector along the swimming direction, and the diffusion coefficient $D$ is assumed to be constant. The concentration of the stratified agent is governed by a convection–diffusion equation:

$$\frac{\partial S}{\partial t} + \boldsymbol{u} \cdot \boldsymbol{\nabla} S = \kappa \nabla^2 S, \tag{2.4}$$

where $\kappa$ denotes the corresponding diffusivity coefficient. Its value ranges from $\sim 10^{-5}$ cm$^2$ s$^{-1}$ for salt to $\sim 10^{-3}$ cm$^2$ s$^{-1}$ for heat.

To facilitate dealing with physical parameters, we non-dimesionalize the equations by scaling length by a characteristic dimension of the chamber $L$, time by $L^2/D$, velocity by $D/L$, cell concentration by its mean value $\bar{n}$, and salinity concentration (or temperature) by its initial difference across the domain $\Delta S$. The resulting set of coupled equations becomes

$$\boldsymbol{\nabla} \cdot \boldsymbol{u} = 0, \tag{2.5}$$

$$\frac{\partial \boldsymbol{u}}{\partial t} + \boldsymbol{u} \cdot \boldsymbol{\nabla} \boldsymbol{u} = -\boldsymbol{\nabla} p_e - Sc(Rn + LeR_s S)\hat{\boldsymbol{z}} + Sc \nabla^2 \boldsymbol{u}, \tag{2.6}$$

https://doi.org/10.1017/jfm.2013.415 Published online by Cambridge University Press

$$\frac{\partial n}{\partial t} + \boldsymbol{u}\cdot\boldsymbol{\nabla} n = -\boldsymbol{\nabla}\cdot(nV_c\boldsymbol{p}) + \nabla^2 n, \tag{2.7}$$

$$\frac{\partial S}{\partial t} + \boldsymbol{u}\cdot\boldsymbol{\nabla} S = Le\nabla^2 S, \tag{2.8}$$

where the dimensionless numbers are defined as follows:

$$Sc = \frac{\nu}{D} \quad \text{(Schmidt number)}, \tag{2.9a}$$

$$Le = \frac{\kappa}{D} \quad \text{(Lewis number)}, \tag{2.9b}$$

$$V_c = \frac{W_c L}{D} \quad \text{(dimensionless swimming speed)}, \tag{2.9c}$$

$$R = \frac{\bar{n}\nu\Delta\rho g L^3}{\rho\nu D} \quad \text{(bioconvection Rayleigh number)}, \tag{2.9d}$$

$$R_s = \frac{g\beta\Delta S L^3}{\nu\kappa} \quad \text{(salinity/temperature Rayleigh number)}, \tag{2.9e}$$

with $\nu$ being the kinematic viscosity.

Here, we assume the cells to be ideal spheres of radius $a$ and mass $m$. The cells are bottom-heavy, so the centre of mass is offset by a distance $h$ from the centre of buoyancy. Utilizing the torque balance between gravity and shear flow and neglecting the inertial effects at the low Reynolds numbers associated with the motility of the cells, the equation for the reorientation rate of the sphere is specified by Pedley & Kessler (1987) as

$$\dot{\boldsymbol{p}} = \frac{1}{2B}\left[\hat{\boldsymbol{z}} - (\hat{\boldsymbol{z}}\cdot\boldsymbol{p})\boldsymbol{p}\right] + \frac{1}{2}\boldsymbol{\omega}\times\boldsymbol{p}, \tag{2.10}$$

where $\boldsymbol{\omega}$ is the local vorticity field and $B = 4\pi\mu a^3/mgh$ is a time scale for gyrotactic reorientation. In dimensionless form, the gyrotactic parameter is given by $G = BD/L^2$ which represents the ratio of reorientation time scale to the time it takes for cells to diffuse across the domain. Based on (2.10), vorticity and gravity orient the spherical cells and direct their swimming trajectories in the bulk flow. However, the complex reorientation of the organisms in the vicinity of the rigid walls is not taken into account by this equation. This effect, as shown by Berke *et al.* (2008), gains significance when the cells are at most about 10 body lengths away form the wall. For the micro-organisms associated with the current study, this distance is about $O(100\ \mu\text{m})$ which is negligible compared to the scale of our problem ($O(10\ \text{cm})$). Thus, we neglect the immediate influence of solid boundaries on the cells' swimming direction.

### 2.2. *Geometry and initial conditions*

The governing equations are numerically integrated in a three-dimensional region bounded by the planes $x = [-\Gamma_h/2, \Gamma_h/2]$, $y = [-\Gamma_h/2, \Gamma_h/2]$ and $z = [0, \Gamma_v]$ where $\Gamma_h$ and $\Gamma_v$ are the aspect ratios of the chamber in the horizontal and vertical directions, respectively. The cell concentration is initialized from a uniform state together with a tiny perturbation to ensure the formation of the plume along the centreline of the chamber,

$$n(\boldsymbol{x}, 0) = 1 + \varepsilon\cos(\pi x)\cos(\pi y), \tag{2.11}$$

https://doi.org/10.1017/jfm.2013.415 Published online by Cambridge University Press

where $\varepsilon = 10^{-8}$. The initial conditions for the fluid velocity and swimming direction are derived from the equilibrium solution as $\boldsymbol{u} = \boldsymbol{0}$ and $\boldsymbol{p} = \hat{z}$. Also, to establish the density stratification, simulations are initialized with a linear salinity profile in the vertical direction as $S = 1 - z$.

## 3. Numerical procedure

To solve the system of equations given by (2.5)–(2.8) and (2.10) we used a highly efficient parallel spectral element code developed to solve the Boussinesq equations (Fischer 1997). The advantage of parallel computing is that it provides us with the capability of simulating bioconvection in large-aspect-ratio chambers with realistic boundary conditions. This code has been used and verified in several numerical simulations of Rayleigh–Bénard convection discussed in the literature (Paul *et al.* 2001, 2003; Karimi & Paul 2012). Also, it has been employed in various simulations of bioconvection phenomenon (Karimi 2012; Karimi & Paul 2013) and its outcomes have been compared with the results of Ghorai & Hill (2007) in terms of the characteristics of the flow and the cell concentration. Although they exhibit agreement qualitatively, a discrepancy is observed in the transient behaviour of the concentration profile which is most likely to stem from the difference in the calculation strategy of the swimming orientation. In order to calculate the swimming direction of the cells, we integrate the reorientation equation at each time step and over the entire domain, while Ghorai & Hill (2007) use the equilibrium values of the swimming vector.

For temporal discretization, third-order Adams–Bashforth time differencing has been used to integrate both the field equations and the reorientation equation with time step of $\Delta t = 10^{-4}$ for small-aspect-ratio chambers and $\Delta t = 10^{-5}$ for larger domains with higher modes of instability. To conserve the magnitude of the swimming direction $\boldsymbol{p}$, a post-stabilization approach has been devised to project the result of time integration onto the invariant set of unit vectors (Ascher & Petzold 1998). Within each spectral element we have used 11th-order polynomials to represent the field variables spatially. Grid independence tests have been performed to ensure the convergence of the results.

## 4. Linear stability analysis

In the absence of stratification, bioconvection causes the formation of plumes which promotes the circulation of the flow and enhances the fluid mixing. But experimental observations (Bearon & Grunbaum 2006) indicate that introducing a salinity gradient suppresses bioconvection, enabling cells to form a dense aggregate on the top surface of the chamber. To investigate this phenomenon analytically, we explore the onset of gyrotactic bioconvection in the presence of a salinity (heat) gradient via classical stability analysis of linearized governing equations.

The system of equations introduced in § 2 has a steady equilibrium solution which in dimensionless form is

$$\boldsymbol{u} = 0, \quad \boldsymbol{p} = \hat{z}, \quad n = N \exp(V_c z), \tag{4.1}$$

where $N = V_c[1 - \exp(-V_c)]$ represents the highest concentration of the cells at the top surface before occurrence of overturning instability. In this section, we assume the fluid layer to be horizontally unbounded, but with a characteristic height of $L$. Thus, in dimensionless form, our domain of study lies between the planes $z = -1, 0$. In order to conform with experimental conditions (cf. Bearon & Grunbaum 2006), we assume the lower boundary in the $z$ direction to be a rigid wall, but the upper one a free surface open to the air. Moreover, no-flux conditions are imposed for the cells at both top and

https://doi.org/10.1017/jfm.2013.415 Published online by Cambridge University Press

bottom boundaries. Hence, the boundary conditions are

$$\boldsymbol{u} = 0, \quad \boldsymbol{J} \cdot \hat{\boldsymbol{z}} = 0 \quad \text{at } z = -1, \tag{4.2}$$

$$\boldsymbol{u} \cdot \hat{\boldsymbol{z}} = 0, \quad \frac{\partial \boldsymbol{u}_h}{\partial z} = 0, \quad \boldsymbol{J} \cdot \hat{\boldsymbol{z}} = 0 \quad \text{at } z = 0, \tag{4.3}$$

where the subscript $h$ denotes the horizontal components. In the laboratory, the effect of the presence of stratification on the bioconvection is investigated inside an experimental tube which is impermeable in terms of salinity transfer. However, the equilibrium solution of the salinity with no-flux boundary conditions yields a constant distribution across the domain. Thus to impose a salinity gradient, in accordance with Bearon & Grunbaum (2006), fixed boundary conditions for $S$ are preferred in this section, leading to a steady linear profile as $S = -z$.

The linear stability of the problem is analysed by adding a perturbation with small amplitude $\epsilon \ll 1$ to the equilibrium state as

$$\boldsymbol{u} = \epsilon \boldsymbol{u}', \quad p_e = p_{equil} + \epsilon p_e', \quad n = N \exp(V_c z) + \epsilon n', \tag{4.4}$$

$$S = -z + \epsilon S', \quad \boldsymbol{p} = \hat{\boldsymbol{z}} + \epsilon \boldsymbol{p}', \tag{4.5}$$

where $p_{equil}$ denotes the pressure distribution at the equilibrium state. By substituting these variables into the governing equations and grouping term at $O(\epsilon)$, the linearized equations are derived as follows:

$$\nabla \cdot \boldsymbol{u}' = 0, \tag{4.6}$$

$$\frac{1}{Sc}\frac{\partial \boldsymbol{u}'}{\partial t} = -\nabla p_e' - (Rn' + LeR_s S')\hat{\boldsymbol{z}} + \nabla^2 \boldsymbol{u}', \tag{4.7}$$

$$\frac{\partial n'}{\partial t} + w' V_c N \exp(V_c z) = -\nabla \cdot (V_c N \exp(V_c z)\boldsymbol{p}' + V_c n' \hat{\boldsymbol{z}} - \nabla n'), \tag{4.8}$$

$$\frac{\partial S'}{\partial t} - w' = Le \nabla^2 S', \tag{4.9}$$

where $w'$ represents the vertical component of $\boldsymbol{u}'$. Also, the reorientation rate equation (2.10) can be linearized as

$$\dot{\boldsymbol{p}}' = -\frac{1}{2G}\left[\boldsymbol{p}' + (\hat{\boldsymbol{z}} \cdot \boldsymbol{p}')\hat{\boldsymbol{z}}\right] + \frac{1}{2}\boldsymbol{\omega}' \times \hat{\boldsymbol{z}}, \tag{4.10}$$

where $\boldsymbol{\omega}' = \nabla \times \boldsymbol{u}'$ indicates the perturbation of vorticity. In order to eliminate pressure, the curl of (4.7) is taken twice, which results in

$$\left(\frac{1}{Sc}\frac{\partial}{\partial t} - \nabla^2\right)\nabla^2 w' = R\nabla_h^2 n' + LeR_s \nabla_h^2 S'. \tag{4.11}$$

Using the decomposition proposed by Hill, Pedley & Kessler (1989), the perturbation quantities can be represented in terms of normal modes as

$$w' = \mathscr{W}(z) f(x, y) \mathrm{e}^{\sigma t}, \quad n' = \mathscr{N}(z) f(x, y) \mathrm{e}^{\sigma t}, \quad S' = \mathscr{S}(z) f(x, y) \mathrm{e}^{\sigma t}, \tag{4.12}$$

where $\sigma$ denotes the growth rate and $f$ is any horizontal function such that $\nabla_h^2 f = -k^2 f$ with $k$ being the wavenumber of the associated mode corresponding to a wavelength $\lambda = 2\pi/k$. Also, we expand the perturbation of the swimming direction vector as $\boldsymbol{p}' = \boldsymbol{\mathcal{P}}(x, y, z)\mathrm{e}^{\sigma t}$. Substituting these decompositions into the linearized

https://doi.org/10.1017/jfm.2013.415 Published online by Cambridge University Press

equations yields the following system of ordinary differential equation (ODEs):

$$\left(\frac{\sigma}{Sc}+k^2-\frac{\mathrm{d}^2}{\mathrm{d}z^2}\right)\left(k^2-\frac{\mathrm{d}^2}{\mathrm{d}z^2}\right)\mathscr{W}=-k^2(R\mathscr{N}+LeR_s\mathscr{S}), \tag{4.13}$$

$$\left(\sigma+V_c\frac{\mathrm{d}}{\mathrm{d}z}+k^2-\frac{\mathrm{d}^2}{\mathrm{d}z^2}\right)\mathscr{N}=V_cN\exp(V_cz)\left[G_m\frac{\mathrm{d}^2}{\mathrm{d}z^2}-G_mk^2-1\right]\mathscr{W}, \tag{4.14}$$

$$\left(\frac{\sigma}{Le}+k^2-\frac{\mathrm{d}^2}{\mathrm{d}z^2}\right)\mathscr{S}=\frac{\mathscr{W}}{Le}, \tag{4.15}$$

with the boundary conditions

$$\mathscr{W}=\frac{\mathrm{d}\mathscr{W}}{\mathrm{d}z}=\frac{\mathrm{d}\mathscr{N}}{\mathrm{d}z}-V_c\,\mathscr{N}=\mathscr{S}=0\quad\text{at } z=-1, \tag{4.16}$$

$$\mathscr{W}=\frac{\mathrm{d}^2\mathscr{W}}{\mathrm{d}z^2}=\frac{\mathrm{d}\mathscr{N}}{\mathrm{d}z}-V_c\,\mathscr{N}=\mathscr{S}=0\quad\text{at } z=0, \tag{4.17}$$

where $G_m=G/(1+2\sigma G)$.

In this section, we attempt to calculate the neutral curves, i.e. the solutions for which the perturbations neither grow nor decay, corresponding to $\mathrm{Re}(\sigma)=0$. Thus we fix all the parameters of the system except one (here chosen to be either $R$ or $R_s$) and seek solutions to the system of ODEs associated with zero growth rate for various values of the wavenumber. The minimum of the curve, often referred to as the critical point, corresponds to the most unstable mode and indicates the threshold for transition to instability.

Using the estimates of the physical parameters for a suspension of alga *C. nivalis* given by Kessler (1986), we employ the following set of dimensionless numbers in accordance with the simulations of Ghorai & Hill (2007):

$$Sc=20,\quad V_c=10,\quad G=0.01, \tag{4.18}$$

to represent the swimming behaviour of the micro-organisms. The diffusivity coefficient of the salt is estimated to be $\kappa=1.5\times10^{-5}$ cm$^2$ s$^{-1}$ (Bearon & Grunbaum 2006) which yields a value of Lewis number $Le=0.03$. Thus, in this case, the destabilizing component (cells) diffuses faster than the stabilizing agent (salinity). On the other hand, the swimming of the same species of micro-organisms in thermally stratified environment corresponds to $Le=3>1$.

The boundary value problem consisting of (4.13)–(4.17) has been solved numerically using MATLAB and the code has been verified by comparing the results with those given by Hill *et al.* (1989) for the case of bioconvection in homogeneous fluid. The computational scheme is iterated until the convergence of the parameter of interest is assured. In figures 1(*a*) and 1(*b*), the corresponding results have been compared with the asymptotic relationship based on the perturbation solution of Bearon & Grunbaum (2006). Their equation for the neutral curve in the $(k,R)$ plane has been derived assuming that: (i) fluid flow does not alter the swimming direction (gravitactic motility); and (ii) both boundaries on the top and bottom surfaces are rigid. To conform with these assumptions for the sake of comparison, we solved the aforementioned boundary value problem with both free and rigid boundary conditions on the top wall. Moreover, a highly stratified fluid column is assumed which corresponds to $R_s=10^6$. The neutral curves plotted in figure 1(*a*) are calculated using a smaller value of $G=10^{-4}$ in order to amplify the upward swimming by reducing the effect of vorticity to reorient the cells. In this case, the asymptotic

https://doi.org/10.1017/jfm.2013.415 Published online by Cambridge University Press

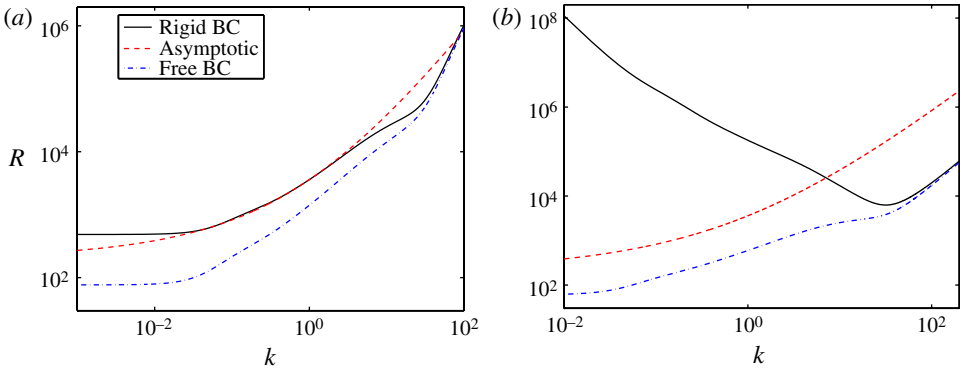



FIGURE 1. (Colour online) Comparison of the neutral curves resulting from the linear stability analysis in the $(k, R)$ plane with the asymptotic solution of Bearon & Grunbaum (2006) for $(a)$ $G = 10^{-4}$ and $(b)$ $G = 0.01$. The results are calculated for both free and rigid boundary conditions on the top surface. The other parameters of the system are $Sc = 20$, $V_c = 10$ and $R_s = 10^6$.

solution under-predicts the critical Rayleigh number at the onset of instability at zero wavenumber, but it shows a good agreement with the results of the current linear stability analysis over a medium range of $k$. This figure also confirms our intuition that the upper no-slip boundary condition is associated with higher values of $R$ at the onset of bioconvection due to inhibition of the lateral movement. This comparison has been repeated in figure 1$(b)$ using the aforementioned value of $G = 0.01$ in order to scrutinize the accuracy of the asymptotic solution when the effect of fluid flow on the cell orientation becomes more dominant. While changing the value of $G$ does not affect the asymptotic curve, it has a significant impact on the neutral curves resulting from the current analysis. In particular, when both boundaries are rigid, the most unstable mode of the system occurs at a non-zero wavenumber ($k_{crit} \approx 31.7$), corresponding to a critical Rayleigh number $R_{crit} \approx 6.3 \times 10^3$. Thus, by increasing $G$ and strengthening the gyrotactic effects, the asymptotic solution becomes inconsistent with the results of the more comprehensive linear stability analysis presented here.

Using the parameter values given in (4.18), the neutral curves are calculated in $(k, R)$ and $(k, R_s)$ planes which are shown in figures 2$(a)$ and 2$(b)$, respectively. As figure 2$(a)$ shows, $R$ is minimized at $k = 0$ for a broad range of $R_s$, corresponding to a critical Rayleigh number $R_{crit} \approx 60$. By increasing $k$, the neutral curves begin to separate, but eventually they converge to a single line at high wavenumbers. Also, figure 2$(b)$ indicates that due to the inhibiting effect of stratification, by increasing the magnitude of $R_s$, the wavelength of the pattern grows up to the horizontal extent of the domain. Indeed, in a highly stratified fluid column with finite width ($\Gamma_h$ in dimensionless form), if the value of $R_s$ is larger than the threshold determined from the neutral curves in the $(k, R_s)$ plane, the pattern will consist of horizontally uniform isosurfaces with wavelength $\lambda \to \Gamma_h$. Conversely, as the magnitude of salinity gradient drops, more complex patterns with smaller $\lambda$ will arise. It is also interesting that regardless of the value of $R$, a second-order decay can be observed in neutral curves in the $(k, R_s)$ plane. This decay is interrupted as the curves reach the maximum attainable wavenumber ($k_c$) and for larger wavenumbers, the system remains stable. Existence of such a cut-off wavenumber is associated with the instability mechanism of the system. In this study, the salinity gradient is devised to have a stabilizing effect

https://doi.org/10.1017/jfm.2013.415 Published online by Cambridge University Press

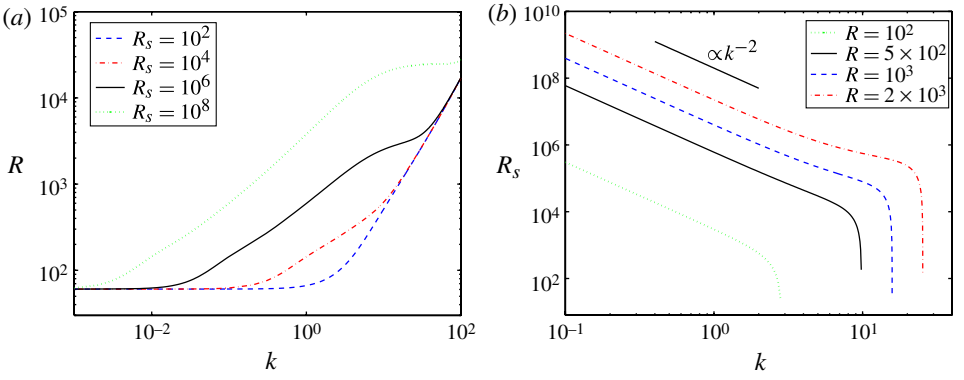



FIGURE 2. (Colour online) The neutral curves resulting from the linear stability analysis in (*a*) the $(k, R)$ plane and (*b*) the $(k, R_s)$ plane. The parameters of the system are $Sc = 20$, $V_c = 10$ and $G = 0.01$.

whereas the bioconvection phenomenon tends to destabilize the system. Thus, the most unstable state is correlated with the occurrence of bioconvection in homogeneous fluid. In this case, the instability triggers a pattern with a wavenumber equal to $k_c$ which for every specific value of $R$ can be derived from the neutral curve in the $(k, R)$ plane corresponding to bioconvection without stratification ($R_s = 0$). It is worth mentioning that the neutral curves at all cases are identical for two different values of Lewis number, $Le = 0.03$ and 3, which indicates the independence of linear stability characteristics from the diffusivity ratio.

## 5. Numerical results

In this section, we simulate the gyrotactic bioconvection in the presence of a linear salinity gradient across the height of a vessel to analyse the effect of stratification on the distribution of the cells. The salinity is considered to be stably stratified, in contrast to the micro-organisms where their initial aggregation on the top layer initiates an overturning instability. In the following, the same characteristic dimensionless parameters of the system have been used as given by (4.18). Also, the value of Rayleigh number is kept constant at $R = 500$ unless stated otherwise. In order to investigate the impact of strength of stratification on the flow regime, we will vary the value of $R_s$ in the range of $10^4$–$10^6$. Using the measures given by Bearon & Grunbaum (2006) for the size of their experimental chamber and the properties of salt and water, these values of salinity Rayleigh number can be related to density gradients of $\approx 10^{-4}$–$10^{-2}$ kg m$^{-4}$ which correspond to the vertical variations in water density in oceanic environments (Yamazaki & Squires 1996).

In the following, the pattern formation of the cell concentration field is illustrated via the horizontal average of $n(x, y, z, t)$, defined as

$$n_{avz}(z, t) = \int_{A_z} n \, \mathrm{d}x \, \mathrm{d}y \tag{5.1}$$

where $A_z$ denotes the horizontal cross-section of the domain at height $z$. As the plume formation and stratification effects occur predominantly at the vertical direction, the space–time plot of $n_{avz}$ depicts the main spatial features of the dynamical behaviour of the system.

https://doi.org/10.1017/jfm.2013.415 Published online by Cambridge University Press

To quantify the spreading of the cells across the domain, we calculate the second moment (Chiam *et al.* 2005) of the cell concentration field,

$$\tilde{M}_n(t) = \frac{\displaystyle\int_V |\boldsymbol{x} - \langle \boldsymbol{x} \rangle|^2 n(\boldsymbol{x}, t)\, \mathrm{d}V}{\displaystyle\int_V n(\boldsymbol{x}, t)\, \mathrm{d}V}. \tag{5.2}$$

Here, $V$ denotes the volume of the chamber and the quantity $\langle \boldsymbol{x} \rangle$ is the instantaneous centre of mass of the cell distribution,

$$\langle \boldsymbol{x} \rangle = \frac{\displaystyle\int_V \boldsymbol{x} n(\boldsymbol{x}, t)\, \mathrm{d}V}{\displaystyle\int_V n(\boldsymbol{x}, t)\, \mathrm{d}V}. \tag{5.3}$$

$\tilde{M}_n(t)$ takes a characteristic value, solely dependent on the geometry of the domain, when the cells are well-mixed and uniformly distributed. In the following figures, the value of $\tilde{M}_n(t)$ is always normalized with respect to the corresponding geometric constant and is denoted by $M_n(t)$ hereafter. Thus, the uniform spreading of the cells is associated with $M_n(t) \sim 1$ and their localization is exhibited through the deviation of $M_n(t)$ from unity. Analogously to the cells' concentration, the uniformity of the salinity distribution can be analysed by calculating the corresponding second moment of the salinity field, $M_s(t)$.

### 5.1. *Effect of salinity Rayleigh number*

First, we explore and categorize different flow regimes by varying the value of salinity Rayleigh number. In order to model an experimental chamber containing a population of micro-organisms suspended in a stratified fluid, we specify no-slip boundary conditions on all material walls except the top one which is considered to be stress-free in order to model the free surface of the bioconvection chamber. The boundary conditions on $n$ and $S$ are such that there be no flux of cells and salinity (or heat) through the walls, thus $\boldsymbol{J} \cdot \hat{\boldsymbol{n}} = 0$ and $\nabla S \cdot \hat{\boldsymbol{n}} = 0$ where $\hat{\boldsymbol{n}}$ is the unit normal to the respective wall. Thus, the insights gained from the linear stability analysis are not applicable here due to difference in salinity boundary conditions. However in the next sections, we will also simulate cases with constant salinity boundary conditions and the compatibility of the results with our analytical study in terms of stability of the patterns will be exhibited. Also, it is noteworthy that on rigid walls where $\boldsymbol{u} = \boldsymbol{0}$, the flux arising from the motility of the cells is balanced with the flux engendered by the diffusion, which in the currently employed model represents the effects of translational Brownian motion and the collision of the cells. Therefore, imposing a no-flux condition for the cells on the boundaries ensures that the micro-organisms do not pass through the wall, either because of their swimming velocity or due to the random walk process.

The first set of simulations has been done on a box domain with aspect ratios $\Gamma_h = \Gamma_v = 1$ with the aforementioned micro-organism characteristic parameters. In this section, the dimensions of the chamber have been non-dimensionalized with respect to the horizontal extent of the domain. The evolution of the horizontal average and the second moment of the cell concentration with time are shown in figures 3 and 4(*a*), respectively, for various values of salinity Rayleigh number. The case of $R_s = 0$ corresponds to the state of no salinity stratification and is characterized by

https://doi.org/10.1017/jfm.2013.415 Published online by Cambridge University Press

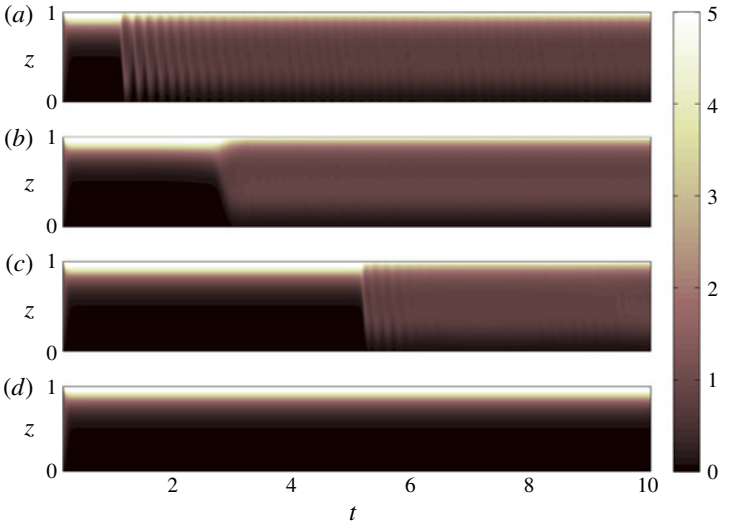



FIGURE 3. (Colour online) Space–time plots of the horizontal average of the cell concentration for (*a*) $R_s = 0$, (*b*) $R_s = 10^4$, (*c*) $R_s = 10^5$ and (*d*) $R_s = 10^6$. The domain aspect ratios are $\Gamma_h = \Gamma_v = 1$ and the Lewis number is $Le = 0.03$.

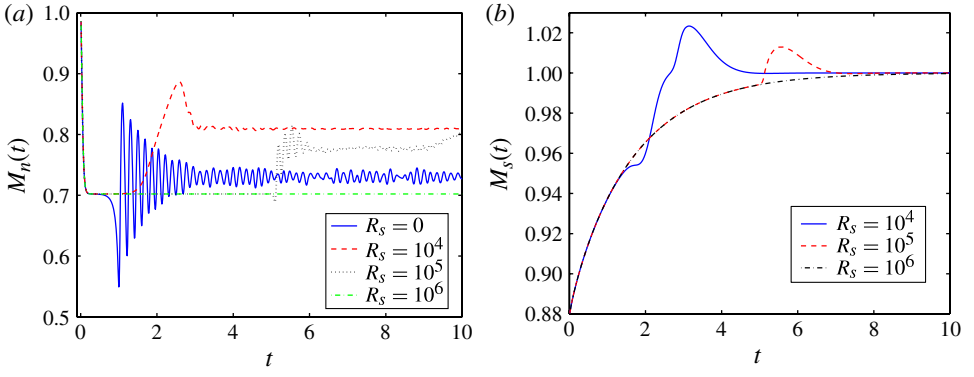



FIGURE 4. (Colour online) Variation of the second moment with time for (*a*) cell concentration, and (*b*) salinity distribution. The domain aspect ratios are $\Gamma_h = \Gamma_v = 1$ and the Lewis number is $Le = 0.03$.

a periodic blob convection regime with diminishing amplitude (see figure 3*a* and supplementary movie 1 available at http://dx.doi.org/10.1017/jfm.2013.415 showing plume dynamics represented via the time evolution of isosurfaces of $n$). When $R_s$ is small, the instability engendered by bioconvection suppresses the stabilizing influence of salinity stratification and the plume dynamics behaves similarly to the case of $R_s = 0$. However, the results demonstrate that for high values of $R_s$, bioconvection is inhibited and the cells aggregate on the top surface of the domain. This accumulation of micro-organisms remains stable as long as the stratification is strong enough to impede the formation of the bioconvective plumes. This transition in the dynamical behaviour of the system can be quantitatively characterized by the buoyancy ratio $R_\rho$

https://doi.org/10.1017/jfm.2013.415 Published online by Cambridge University Press

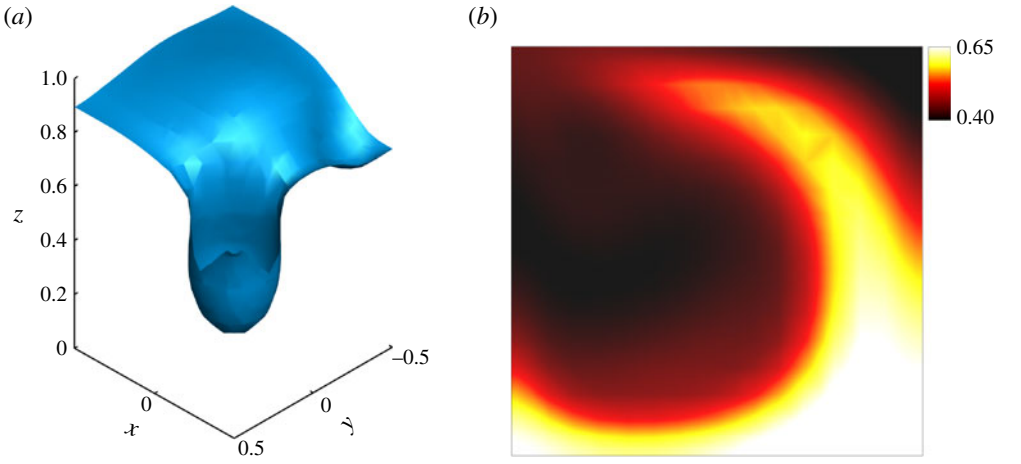



FIGURE 5. (Colour online) (*a*) Gyrotactic plume represented as an isosurface of $n = 2$, and (*b*) salinity profile at the vertical midplane. The snapshots are taken at $t = 2.8$. The domain aspect ratios are $\Gamma_h = \Gamma_v = 1$ with parameters $Le = 0.03$ and $R_s = 10^4$.

which represents the relative importance of salinity and cell concentration buoyant forces, and is given by

$$R_\rho = \frac{R_s\, Le \langle \Delta S \rangle}{R \langle \Delta n \rangle}, \tag{5.4}$$

where $\langle \Delta S \rangle$ and $\langle \Delta n \rangle$ stand for the average variation of dimensionless values of concentration of cells and salinity across the domain. This notion has been widely used in the context of thermosolutal double diffusion to identify different regimes of the flow (Turner 1985). To evaluate this quantity approximately, we assume a linearly stratified bioconvective chamber at the static equilibrium state. For such a system, the equilibrium distributions in dimensionless form are (Ghorai & Hill 2007)

$$n_s(z) = \frac{V_c \Gamma_v \exp(V_c z)}{\exp(V_c \Gamma_v) - 1}, \quad S_s(z) = 1 - z. \tag{5.5}$$

Thus, the average variations can be approximated as $\langle \Delta n \rangle \sim V_c \Gamma_v$ and $\langle \Delta S \rangle \sim 1$. Using these values, the buoyancy ratio can be evaluated as

$$R_\rho = \frac{R_s\, Le}{R V_c \Gamma_v}. \tag{5.6}$$

Based on the values associated with this case, for $R_s = 10^4$, $R_\rho < 1$, for $R_s = 10^5$, $R_\rho \sim O(1)$, and for $R_s = 10^6$, $R_\rho > 1$ which justifies the physical interaction of two stratification agents. In both cases $R_s = 10^4$ and $10^5$ a meandering instability occurs in which the plume moves toward one of the sidewalls where it settles as a quasi-steady state (see figure 5*a* illustrating an isosurface of $n$ for the case of $R_s = 10^4$). Comparing these cases reveals how by increasing the strength of the salinity gradient, the onset of instability and the consequent plume formation is delayed.

The variation of $M_s(t)$ with time for the salinity profile is shown in figure 4(*b*). For the cases of $R_s = 10^4$ and $10^5$, the spatial distribution of salinity is slaved to the shape of the plume of cells, leading to the formation of high-salinity regions along the

https://doi.org/10.1017/jfm.2013.415 Published online by Cambridge University Press

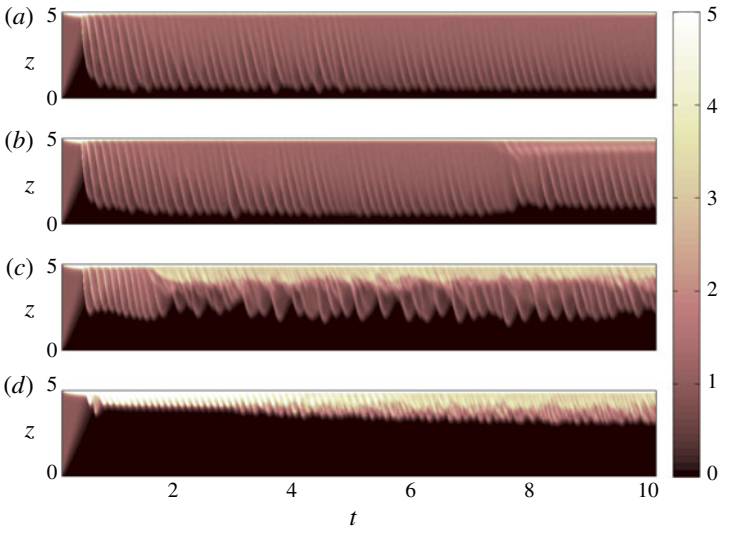



FIGURE 6. (Colour online) Space–time plots of the horizontal average of the cell concentration for (*a*) $R_s = 0$, (*b*) $R_s = 10^4$, (*c*) $R_s = 10^5$ and (*d*) $R_s = 10^6$. The domain aspect ratios are $\Gamma_h = 1$ and $\Gamma_v = 5$ and the Lewis number is $Le = 0.03$.

vertical edges of the domain and causing $M_s(t)$ to take values larger than one. As an example, a snapshot of the vertical distribution of salinity at the midplane for the case of $R_s = 10^4$ is demonstrated in figure 5(*b*). On the other hand, in the case of $R_s = 10^6$, the bioconvection is suppressed and the only mechanism of salinity transport is pure diffusion which is manifested by exponential growth of the corresponding $M_s(t)$ with time.

A similar set of simulations has been performed using a larger domain size with aspect ratios $\Gamma_h = 1$ and $\Gamma_v = 5$. The corresponding results are portrayed in figures 6 and 7. As it is evident from the time variation of the case with $R_s = 0$, the plume in deep chambers is more prone to instability and exhibits more fluctuating behaviour. By increasing the value of $R_s$, an analogous transition can be observed from no effect on the cell distribution to hindering bioconvection. Also, it is noteworthy that due to the larger height of the domain, the distinction between values of $M_n(t)$ for different regimes of stratification is more dramatic than the previous case. In particular, occurrence of meandering instability leads to the aggregation of the cells in the corners of the top surface which in turn triggers large dips in the temporal profile of $M_n(t)$. The space–time plots illustrated in figure 6 delineate the spatiotemporal plume formation process. For $R_s = 10^4$, the height of plume is almost unchanged by the salinity buoyancy force. But in the case of larger $R_s$, the plume extends only to a fraction of chamber's depth while deviating toward the sidewalls instead of evolving along the centreline. The temporal behaviour of the salinity distribution for this case is depicted in figure 7(*b*). Similar to the case with $\Gamma_v = 1$, when $R_s$ is small, bioconvection causes salinity to concentrate around the vertical edges of the chamber and ultimately, the combined effects of convection and diffusion make the suspension solutally uniform. To elaborate this process, snapshots of the plume of micro-organisms and the vertical distribution of salinity at the midplane for the case of $R_s = 10^4$ are shown in figure 8 at various times (see also supplementary movie 2

https://doi.org/10.1017/jfm.2013.415 Published online by Cambridge University Press

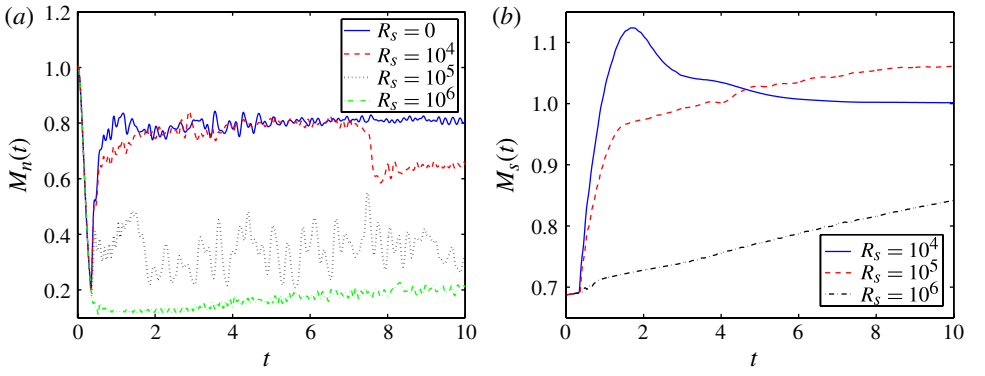



FIGURE 7. (Colour online) Variation of the second moment with time for (*a*) cell concentration, and (*b*) salinity distribution. The domain aspect ratios are $\Gamma_h = 1$ and $\Gamma_v = 5$ and the Lewis number is $Le = 0.03$.

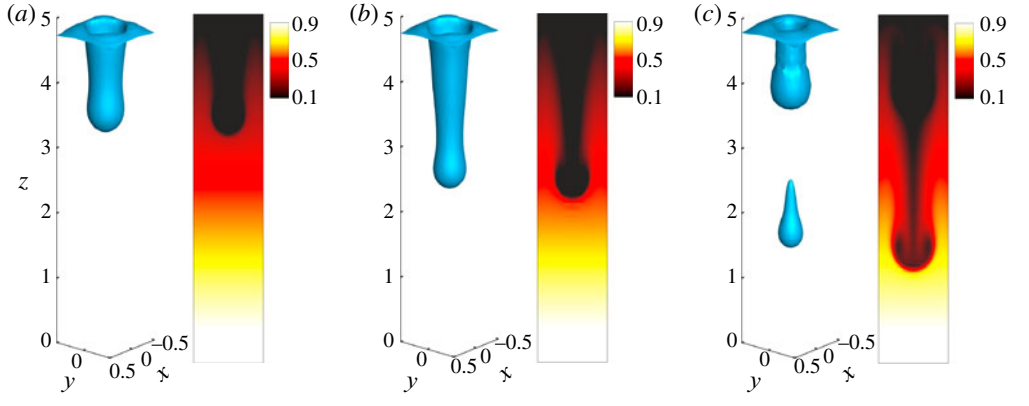



FIGURE 8. (Colour online) Gyrotactic plumes represented as isosurfaces of $n = 3$ and salinity profiles at the vertical midplane. The snapshots are taken at (*a*) $t = 0.36$, (*b*) $t = 0.39$ and (*c*) $t = 0.46$. The domain aspect ratios are $\Gamma_h = 1$ and $\Gamma_v = 5$ with parameters $Le = 0.03$ and $R_s = 10^4$.

showing the temporal evolution of isosurfaces of $n$ and vertical distribution of $S$). By increasing $R_s$, bioconvection is inhibited and salinity diffuses slowly with an exponent that is about one order of magnitude smaller than the corresponding case in the small chamber with $\Gamma_v = 1$.

### 5.2. *Effect of Lewis number*

In order to analyse the effect of diffusivity ratio, we repeated the simulations with similar boundary conditions and the same set of parameters except the Lewis number which was chosen to be $Le > 1$ (corresponding to thermal stratification). Figure 9(*a*) depicts the space–time plot of $n_{avz}$ for a suspension of cells in a box with aspect ratios $\Gamma_h = \Gamma_v = 1$ with $R_s = 10^4$ and $Le = 3$ which yields the same buoyancy ratio as the case of $R_s = 10^6$ and $Le = 0.03$. In this case, the temperature profile equilibrates rapidly due to high thermal diffusivity, leaving no impact on the bioconvection and the qualitative characteristics of the plume dynamics. As demonstrated in figure 10, within

https://doi.org/10.1017/jfm.2013.415 Published online by Cambridge University Press

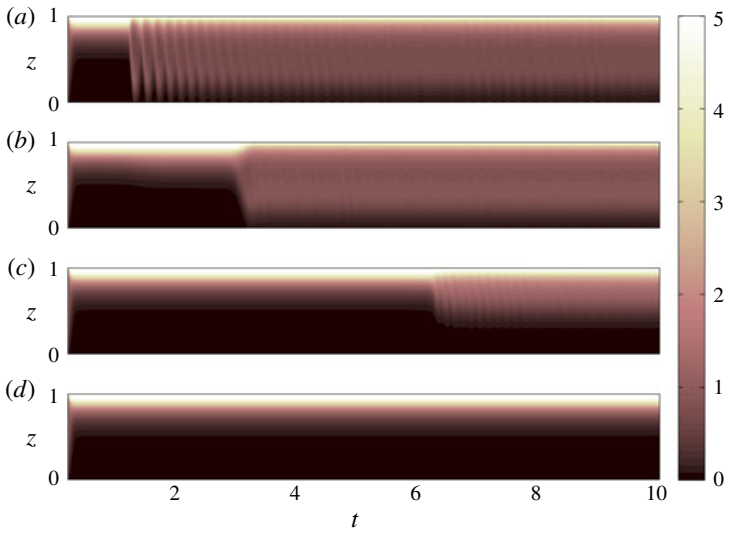



FIGURE 9. (Colour online) Space–time plots of the horizontal average of the cell concentration for (*a*) no-flux ($R_s = 10^4$), (*b*) no-flux ($R_s = 10^5$), (*c*) fixed ($R_s = 10^4$) and (*d*) fixed ($R_s = 2 \times 10^4$) thermal boundary conditions in the $z$ direction. The domain aspect ratios are $\Gamma_h = \Gamma_v = 1$ and the Lewis number is $Le = 3$.

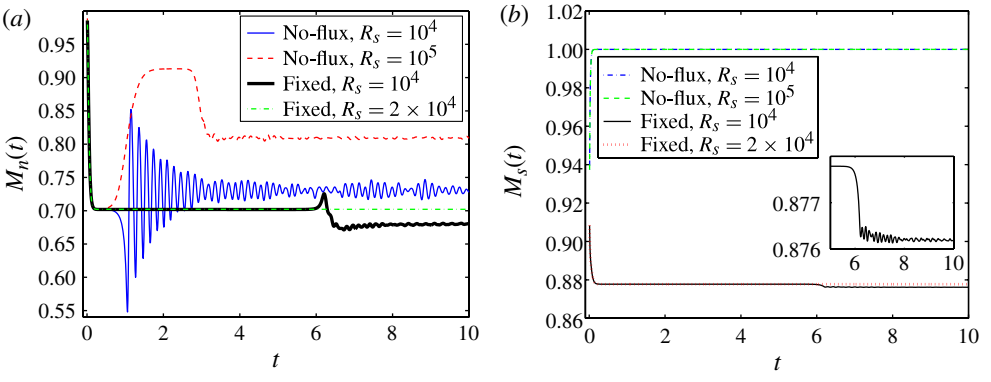



FIGURE 10. (Colour online) Temporal variation of the second moment of distribution of (*a*) cells, and (*b*) stratification agent for different thermal boundary conditions and salinity Rayleigh numbers. The inset in (*b*) magnifies the small fluctuations in the temporal variation of $M_s(t)$ for the case of $R_s = 10^4$ with fixed boundary conditions. The domain aspect ratios are $\Gamma_h = \Gamma_v = 1$ and the Lewis number is $Le = 3$.

short interval of time, the second moment of temperature grows exponentially toward the uniform state and afterwards the corresponding buoyancy force vanishes. Similar results have been obtained with higher values of $R_s$ (see figure 9*b* for the case of $R_s = 10^5$) and in deeper chambers. Fitting the variation of $M_s(t)$ onto an exponential curve yields an exponent which is about 100 times larger than the respective exponent for the case of $Le = 0.03$ which can be rationalized by considering the ratio of the two Lewis numbers. Thus, in the case of $Le > 1$ with thermally insulated boundaries, the

https://doi.org/10.1017/jfm.2013.415 Published online by Cambridge University Press

temperature is homogenized via pure diffusion in a time scale much smaller than that of bioconvection without any implications for the evolution of the cell plumes.

The effect of stratification on the bioconvection in the case of $Le > 1$ is further investigated by imposing a constant temperature on the top and bottom surfaces of the domain instead of no-flux boundary conditions. Although this choice of Dirichlet boundaries maintains the persistent pycnoclines over the course of the simulation, it is not physically compatible with the conditions actually found in the experiment as noted by Bearon & Grunbaum (2006). However, it can be considered as a simplified model of pycnoclines in natural environments which continue to exist over long time scales. We impose the values of the stratification agent as $S(z = 0) = 1$ and $S(z = 1) = 0$ to establish a linear temperature profile at the equilibrium state, similar to the one used in § 4 for the linear stability analysis. Conducting the simulations in a box with unity aspect ratios, similar to the previous ones, allows the pattern formation with maximum wavelength $\lambda = 1$ corresponding to $k = 2\pi$. Using the neutral curves given in figure 2(*b*), the transition salinity Rayleigh number can be derived for this circumstance as $R_{s,c} = 1.89 \times 10^4$. Thus, utilizing the fixed-temperature boundary conditions, two sets of simulations were performed to investigate the spatiotemporal dynamics of the system as $R_s$ passes the transition threshold. The corresponding space–time plots of $n_{avz}$ for the cases of $R_s = 10^4$ and $2 \times 10^4$ are shown in figures 9(*c*) and 9(*d*), respectively. When $R_s < R_{s,c}$, the existence of a persistent temperature gradient inhibits the formation of a plume for a longer interval of time and constrains its vertical extent. Nonetheless, bioconvection is eventually developed via a meandering instability in which the blob of cells is formed around one of the corners. In this case, the final state of the system corresponds to an inclined plume which shows small fluctuations with diminishing amplitude. However in the case of $R_s > R_{s,c}$, the thermal buoyancy force is sufficiently strong to hinder the bioconvective instability, leading to the formation of persistent cell aggregates in the top layer. These dynamical events have also been reflected in the temporal variation of the second moment of distribution of cells and temperature as shown in figure 10. In the case of $R_s = 10^4$, these quantities settle on their static equilibrium values until bioconvection occurs, causing them to move toward a new quasi-steady condition while exhibiting small fluctuations due to blob convection. But for larger values of $R_s$, due to suppression of bioconvection, no dynamical variation is observed in the temporal behaviour of $M_n(t)$ and $M_s(t)$.

### 5.3. *Effect of the upper boundary*

In this section, we analyse the effect of the top surface boundary condition on the characteristics of the bioconvection and its interaction with density stratification. Because in actual experimental conditions, the upper surfaces of Petri dishes used to investigate bioconvection are open to the air, the choice of a stress-free upper boundary appears to be more plausible. However, it has been argued (Hill *et al.* 1989) that the collection of the algal cells forms a packed layer at the top which acts like a rigid surface. As indicated in § 4 via linear stability analysis, imposing a no-slip boundary condition on the upper surface artificially suppresses lateral movement and impedes the occurrence of bioconvection instability. To gain further insight regarding this effect, multiple simulations were conducted in a box domain with aspect ratios $\Gamma_h = \Gamma_v = 1$. The setting and parameters of the system are the same as those given in § 5.1 except Rayleigh number which is raised to a higher value of $R = 2000$ in order to overcome the inhibiting effect of the no-slip upper boundary. Figure 11 depicts the corresponding space–time plots of $n_{avz}$ for various values of $R_s$. Also, the variation of the second

https://doi.org/10.1017/jfm.2013.415 Published online by Cambridge University Press

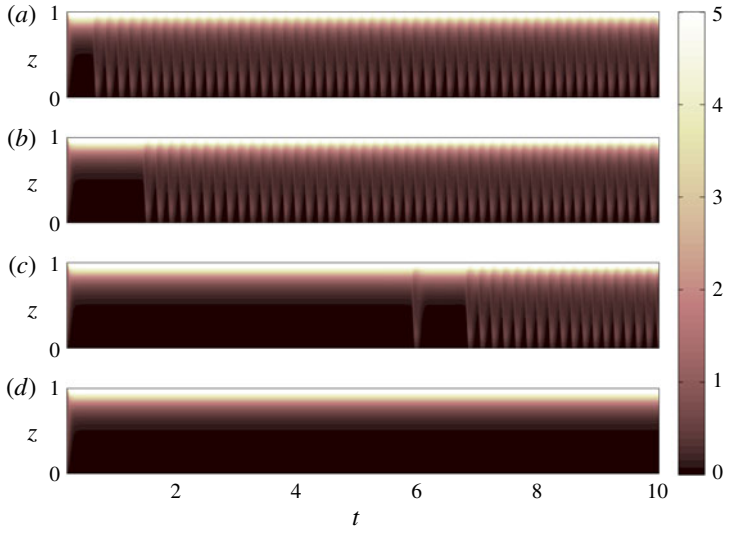



FIGURE 11. (Colour online) Space–time plots of the horizontal average of the cell concentration in the case of a domain with upper rigid boundary for (*a*) $R_s = 0$, (*b*) $R_s = 10^4$, (*c*) $R_s = 10^5$ and (*d*) $R_s = 10^6$. The domain aspect ratios are $\Gamma_h = \Gamma_v = 1$ and the Rayleigh number and Lewis number are $R = 2000$ and $Le = 0.03$, respectively.

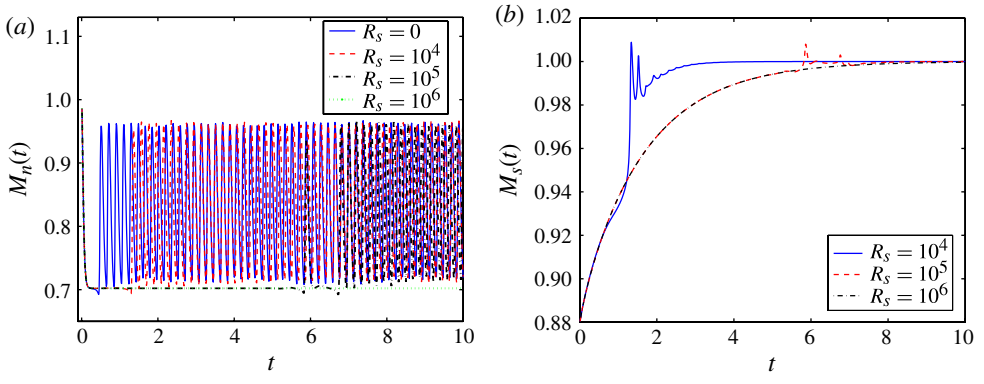



FIGURE 12. (Colour online) Variation of the second moment with time for (*a*) cell concentration, and (*b*) salinity distribution in the case of a domain with upper rigid boundary. The domain aspect ratios are $\Gamma_h = \Gamma_v = 1$ and the Rayleigh number and Lewis number are $R = 2000$ and $Le = 0.03$, respectively.

moment of the cell concentration and salinity distribution with time is illustrated in figure 12. In the case of no salinity gradient, the final state of the system is periodic with a period of approximately 0.18 dimensionless time units. The no-slip boundary conditions for both the top and bottom horizontal planes constrain the flux of the cells to move chiefly in the vertical direction and leads to the formation of two analogous recirculating zones along the vertical extent of the domain. Similar to the results presented in § 5.1, by increasing the value of $R_s$ and strengthening the salinity gradient, the onset of bioconvection instability is postponed. In the case of $R_s = 10^6$ (associated

https://doi.org/10.1017/jfm.2013.415 Published online by Cambridge University Press

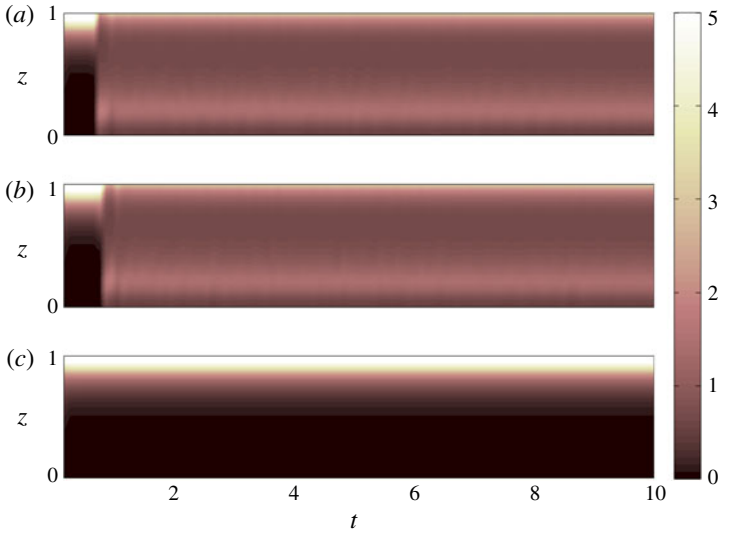



FIGURE 13. (Colour online) Space–time plots of the horizontal average of the cell concentration in the case of a periodic domain for (*a*) $R_s = 0$, (*b*) $R_s = 10^4$ and (*c*) $R_s = 10^5$. The domain aspect ratios are $\Gamma_h = 10$ and $\Gamma_v = 1$ and the Lewis number is $Le = 0.03$.

with $R_\rho > 1$) the bioconvection remains suppressed over the course of the simulation and the cells form a thick layer on the top surface. It can be inferred from the results that regardless of the type of boundary condition imposed on the top surface, the criterion of the buoyancy ratio can be used in order to characterize the interplay of bioconvection and density stratification.

### 5.4. *Periodic domain*

Hitherto, the combined effects of bioconvection and stratification have been analysed in small domains with rigid sidewalls as a model of an experimental chamber. But in environmental conditions, the interaction between the motile micro-organisms and pycnoclines occurs across much larger length scales accommodating a multitude of plumes. To investigate this issue, we conducted several simulations in a horizontally extended large domain with aspect ratios $\Gamma_h = 10$ and $\Gamma_v = 1$. In this section, the aspect ratios are calculated by taking the vertical extent of the domain as the characteristic length scale. Also, the boundary conditions on the sidewalls have been chosen to be periodic in order to represent a realistic environmental region. In the vertical direction, the boundary conditions for velocity and cell concentration are unchanged, while in order to maintain persistent pycnoclines, fixed values of salinity have been imposed on the top and bottom surfaces. The space–time plots of $n_{avz}$ illustrating the dynamical variations of the system for various values of $R_s$ are shown in figure 13. In the case of $R_s = 0$, due to the formation of several plumes after occurrence of the overturning instability, the dispersion of micro-organisms across the domain is amplified, leading to a more uniform distribution of $n_{avz}$ in the $z$ direction. The same conclusion can be inferred from the variation of $M_n(t)$ as shown in figure 14(*a*). By increasing the strength of stratification, we first observe a delay in development of bioconvection and finally for $R_s = 10^5$ it ceases to exist. This behaviour can be rationalized by considering the associated transition salinity Rayleigh

https://doi.org/10.1017/jfm.2013.415 Published online by Cambridge University Press

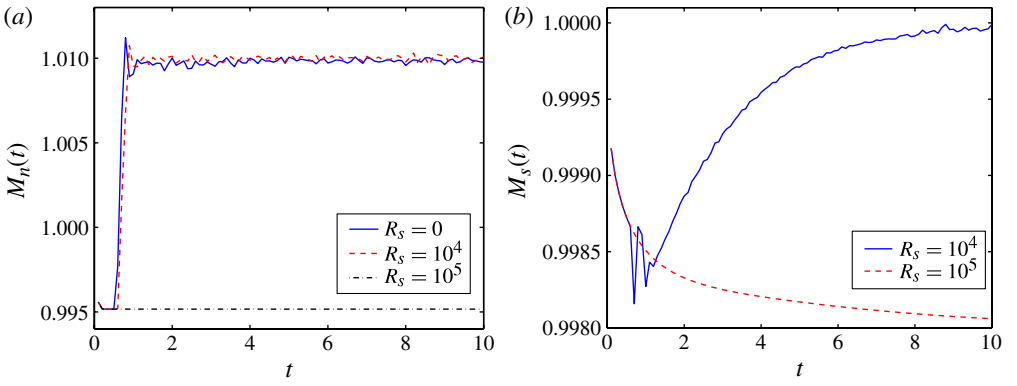



FIGURE 14. (Colour online) Variation of the second moment with time for (*a*) cell concentration, and (*b*) salinity distribution in the case of a periodic domain. The domain aspect ratios are $\Gamma_h = 10$ and $\Gamma_v = 1$ and the Lewis number is $Le = 0.03$.

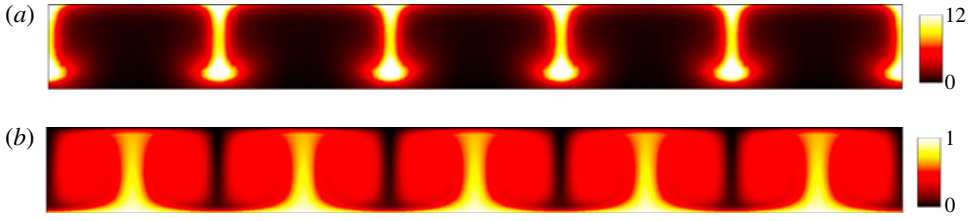



FIGURE 15. (Colour online) Snapshots of (*a*) cell concentration, and (*b*) salinity profile at the vertical midplane of the periodic domain taken at $t = 10$. The domain aspect ratios are $\Gamma_h = 10$ and $\Gamma_v = 1$ and the Lewis number is $Le = 0.03$.

number for this case. In order to derive this quantity via linear stability analysis, we need the wavelength of the pattern formed across the fluid layer which can be inferred from the profiles of the cell concentration and salinity at the vertical midplane of the domain as shown in figure 15. These snapshots indicate that in the case of $R_s = 10^4$, $\lambda \approx 2$ corresponding to a wavenumber value of $k \approx \pi$. Using the neutral curves illustrated in figure 2(*b*), the transition threshold for this circumstance can be calculated as $R_{s,c} = 6.82 \times 10^4$. Thus, the outcomes of simulations are compatible with the insights gained from the stability analysis of the linearized problem. Formation of several plumes in such large systems creates highly convective flows, affecting the distribution of salinity as demonstrated in figure 14(*b*). For $R_s = 10^4$ these circulatory flows drive the salinity toward a uniform distribution, while in the case of $R_s = 10^5$ the second moment of salinity converges to a steady-state value corresponding to the equilibrium linear distribution of the stratification agent along the vertical direction.

## 6. Conclusions

In this work, for the first time, we have presented a linear stability analysis as well as a three-dimensional computational study of gyrotactic bioconvection in the presence of stratification arising from the initially stable solutal/thermal gradients in the vertical direction. We studied the stability of the system analytically and derived the neutral curves corresponding to zero growth rate for various values of $R$ and

https://doi.org/10.1017/jfm.2013.415 Published online by Cambridge University Press

$R_s$. Also, using the results of large-scale numerical simulations, we examined the effects of three key parameters of the problem: the chamber size, the salinity Rayleigh number, and the Lewis number. In case of $Le < 1$ with solutally insulated boundaries, the buoyancy ratio was identified as the characteristic parameter to determine if the salinity gradient is capable of suppressing the bioconvective plumes. Also, it was shown that $R_\rho$ remains the key parameter in both cases of free and rigid upper boundaries. In contrast, when the stratified agent diffuses faster than the cells ($Le > 1$), bioconvection was shown to continue thriving regardless of the magnitude of $R_s$ or the size of the chamber, provided that the boundaries are thermally insulated. This is due to the fact that in this case, the temperature distribution becomes uniform in a short time scale and thus the effects of stratification disappear. However in the case of constant-temperature boundary conditions, associated with more persistent pycnoclines, it was found that there is a critical value of $R_s$, indicating the required strength of the density gradient to inhibit bioconvection which can be derived from the neutral curves resulting from the linear stability analysis. Also, we analysed more environmentally realistic conditions by simulating the governing equations in a large domain with periodic sidewalls. The results indicate that when the value of the corresponding salinity Rayleigh number is less than the transition threshold, small-wavelength patterns consisting of several plumes will be formed.

In this study, we assumed a deterministic micro-organism swimming direction with isotropic diffusivity tensor. Although using this model, we could capture the essential characteristics of the flow and the plume dynamics, more accurate quantification requires utilizing more advanced models to include the effects of randomness in the cells' swimming trajectory. An area of future research could be the incorporation of stochastic swimming models using a Smoluchowski equation (cf. Saintillan & Shelley 2008) into the numerical simulation of gyrotaxis. This approach offers a more consistent framework in order to model the randomizing process in the motility of the cells and to account for the stresses induced in the flow field by swimming micro-organisms. In addition, experimental observations have demonstrated that most of the micro-organisms have elongated bodies which profoundly affect their swimming direction in extensional flows. It would be interesting to study the impact of cell eccentricity on plume formation and other characteristics of bioconvection in stratified environments.

## Acknowledgements

The computations were conducted using the resources of the Center for Research Computing at the University of Notre Dame and the research was supported by NSF Grants CBET-1150348-CAREER and CBET-1066545, and by Lilly Endowment, Inc. Grant No. 2004 1572-000.

## Supplementary movies

Supplementary movies are available at http://dx.doi.org/10.1017/jfm.2013.415.

## REFERENCES

ALLDREDGE, A. L. & GOTSCHALK, C. C. 1989 Direct observations of the mass flocculation of diatom blooms: characteristics, settling velocities and formation of diatom aggregates. *Deep-Sea Res.* A **36** (2), 159–171.

ARDEKANI, A. M. & STOCKER, R. 2010 Stratlets: low Reynolds number point-force solutions in a stratified fluid. *Phys. Rev. Lett.* **105** (8), 084502.

https://doi.org/10.1017/jfm.2013.415 Published online by Cambridge University Press

ASCHER, U. M & PETZOLD, L. R. 1998 *Computer Methods for Ordinary Differential Equations and Differential-Algebraic Equations*. Society for Industrial and Applied Mathematics.

BEARON, R. N., BEES, M. A. & CROZE, O. A. 2012 Biased swimming cells do not disperse in pipes as tracers: a population model based on microscale behaviour. *Phys. Fluids* **24**, 121902.

BEARON, R. N. & GRUNBAUM, D. 2006 Bioconvection in a stratified environment: experiments and theory. *Phys. Fluids* **18** (12), 127102.

BEARON, R. N., HAZEL, A. L. & THORN, G. J. 2011 The spatial distribution of gyrotactic swimming micro-organisms in laminar flow fields. *J. Fluid Mech.* **680**, 602–635.

BEES, M. A. & HILL, N. A. 1997 Wavelengths of bioconvection patterns. *J. Expl Biol.* **200**, 1515–1526.

BERGSTRÖM, B. & STRÖMBERG, J. O. 1997 Behavioural differences in relation to pycnoclines during vertical migration of the euphausiids *Meganyctiphanes norvegica* (m. sars) and *Thysanoessa raschii* (m. sars). *J. Plankton Res.* **19** (2), 255–261.

BERKE, A. P., TURNER, L., BERG, H. C. & LAUGA, E. 2008 Hydrodynamic attraction of swimming microorganisms by surfaces. *Phys. Rev. Lett.* **101**, 038102.

CHIAM, K. H., CROSS, M. C., GREENSIDE, H. S. & FISCHER, P. F. 2005 Enhanced tracer transport by the spiral defect chaos state of a convecting fluid. *Phys. Rev.* E **71** (3), 036205.

DOOSTMOHAMMADI, A., STOCKER, R. & ARDEKANI, A. M. 2012 Low-Reynolds-number swimming at pycnoclines. *Proc. Natl Acad. Sci. USA* **109** (10), 3856–3861.

FISCHER, P. F. 1997 An overlapping Schwarz method for spectral element solution of the incompressible Navier–Stokes equations. *J. Comput. Phys.* **133**, 84–101.

GHORAI, S. & HILL, N. A. 2000 Periodic arrays of gyrotactic plumes in bioconvection. *Phys. Fluids* **12** (1), 5–22.

GHORAI, S. & HILL, N. A. 2007 Gyrotactic bioconvection in three dimensions. *Phys. Fluids* **19** (5), 054107.

GHORAI, S., PANDA, M. K. & HILL, N. A. 2010 Bioconvection in a suspension of isotropically scattering phototactic algae. *Phys. Fluids* **22**, 071901.

HERSHBERGER, P. K., RENSEL, J. E., MATTER, A. L. & TAUB, F. B. 1997 Vertical distribution of the chloromonad flagellate *Heterosigma carterae* in columns: implications for bloom development. *Can. J. Fish. Aquat. Sci.* **54** (10), 2228–2234.

HILL, N. A. & BEES, M. A. 2002 Taylor dispersion of gyrotactic swimming micro-organisms in a linear flow. *Phys. Fluids* **14**, 2598–2605.

HILL, N. A. & PEDLEY, T. J. 2005 Bioconvection. *Fluid Dyn. Res.* **37** (1–2), 1–20.

HILL, N. A., PEDLEY, T. J. & KESSLER, J. O. 1989 Growth of bioconvection patterns in a suspension of gyrotactic micro-organisms in a layer of finite depth. *J. Fluid Mech.* **208**, 509–543.

HILLESDON, A. J. & PEDLEY, T. J. 1996 Bioconvection in suspensions of oxytactic bacteria: linear theory. *J. Fluid Mech.* **324**, 223–259.

HILLESDON, A. J., PEDLEY, T. J. & KESSLER, J. O. 1995 The development of concentration gradients in a suspension of chemotactic bacteria. *Bull. Math. Biol.* **57**, 299–344.

HOPKINS, M. M. & FAUCI, L. J. 2002 A computational model of the collective fluid dynamics of motile micro-organisms. *J. Fluid Mech.* **455**, 149–174.

HUPPERT, H. E. & TURNER, J. S. 1981 Double-diffusive convection. *J. Fluid Mech.* **106**, 299–329.

JEPHSON, T. & CARLSSON, P. 2009 Species- and stratification-dependent diel vertical migration behaviour of three dinoflagellate species in a laboratory study. *J. Plankton Res.* **31** (11), 1353–1362.

KARIMI, A. 2012 Gaining new insights into spatiotemporal chaos with numerics. PhD thesis, Virginia Polytechnic Institute and State University.

KARIMI, A. & PAUL, M. R. 2012 Quantifying spatiotemporal chaos in Rayleigh–Bénard convection. *Phys. Rev.* E **85** (4), 046201.

KARIMI, A. & PAUL, M. R. 2013 Bioconvection in spatially extended domains. *Phys. Rev.* E **87** (5), 053016.

KESSLER, J. O. 1984 Gyrotactic buoyant convection and spontaneous pattern formation in algal cell cultures. In *Non-Equilibrium Cooperative Phenomena in Physics and Related Fields* (ed. M. G. Velarde), pp. 241–248. Plenum.

https://doi.org/10.1017/jfm.2013.415 Published online by Cambridge University Press

KESSLER, J. O. 1985 Hydrodynamic focusing of motile algal cells. *Nature* **313** (5999), 218–220.

KESSLER, J. O. 1986 Individual and collective fluid-dynamics of swimming cells. *J. Fluid Mech.* **173**, 191–205.

LOEFER, J. B. & MEFFERD, R. B. 1952 Concerning pattern formation by free-swimming microorganisms. *Am. Nat.* **86** (830), 325–329.

MANELA, A. & FRANKEL, I. 2003 Generalized taylor dispersion in suspensions of gyrotactic swimming micro-organisms. *J. Fluid Mech.* **490**, 99–127.

MENDELSON, N. H. 1999 *Bacillus subtilis* macrofibres, colonies and bioconvection patterns use different strategies to achieve multicellular organization. *Environ. Microbiol.* **1** (6), 471–477.

PAUL, M. R., CHIAM, K. H., CROSS, M. C., FISCHER, P. F. & GREENSIDE, H. S. 2003 Pattern formation and dynamics in Rayleigh–Bénard convection: numerical simulations of experimentally realistic geometries. *Physica* D **184**, 114–126.

PAUL, M. R., CROSS, M. C., FISCHER, P. F. & GREENSIDE, H. S. 2001 Power-law behaviour of power spectra in low Prandtl number Rayleigh–Bénard convection. *Phys. Rev. Lett.* **87** (15), 154501.

PEDLEY, T. J., HILL, N. A. & KESSLER, J. O. 1988 The growth of bioconvection patterns in a uniform suspension of gyrotactic microorganisms. *J. Fluid Mech.* **195**, 223–237.

PEDLEY, T. J. & KESSLER, J. O. 1987 The orientation of spheroidal microorganisms swimming in a flow field. *Proc. R. Soc. Lond.* B **231** (1262), 47–70.

PEDLEY, T. J. & KESSLER, J. O. 1990 A new continuum model for suspensions of gyrotactic microorganisms. *J. Fluid Mech.* **212**, 155–182.

PEDLEY, T. J. & KESSLER, J. O. 1992 Hydrodynamic phenomena in suspensions of swimming microorganisms. *Annu. Rev. Fluid Mech.* **24**, 313–358.

PLESSET, M. S. & WINET, H. 1974 Bioconvection patterns in swimming microorganism cultures as an example of Rayleigh–Taylor instability. *Nature* **248** (5447), 441–443.

SAINTILLAN, D. & SHELLEY, M. J. 2008 Instabilities and pattern formation in active particle suspensions: kinetic theory and continuum simulations. *Phys. Rev. Lett.* **100**, 178103.

SHERMAN, B. S., WEBSTER, I. T., JONES, G. J. & OLIVER, R. L. 1998 Transitions between *Aulacoseira* and *Anabaena* dominance in a turbid river weir pool. *Limnol. Oceanogr.* **43** (8), 1902–1915.

SMAYDA, T. J. 1997 Harmful algal blooms: their ecophysiology and general relevance to phytoplankton blooms in the sea. *Limnol. Oceanogr.* **42** (5), 1137–1153.

THORN, G. J. & BEARON, R. N. 2010 Transport of spherical gyrotactic organisms in general three-dimensional flow fields. *Phys. Fluids* **22** (4), 041902.

TURNER, J. S. 1973 *Buoyancy Effects in Fluids*. Cambridge University Press.

TURNER, J. S. 1985 Multicomponent convection. *Annu. Rev. Fluid Mech.* **17**, 11–44.

WILLE, J. J. & EHRET, C. F. 1968 Circadian rhythm of pattern formation in populations of a free-swimming organism, *Tetrahymena*. *J. Eukaryot. Microbiol.* **15** (4), 789–792.

YAMAMOTO, Y., OKAYAMA, T., SATO, K. & TAKAOKI, T. 1992 Relation of pattern-formation to external conditions in the flagellate, *Chlamydomonas-Reinhardtii*. *Eur. J. Protistol.* **28** (4), 415–420.

YAMAZAKI, H. & SQUIRES, K. D. 1996 Comparison of oceanic turbulence and copepod swimming. *Mar. Ecol. Prog. Ser.* **14** (1), 299–301.

https://doi.org/10.1017/jfm.2013.415 Published online by Cambridge University Press